

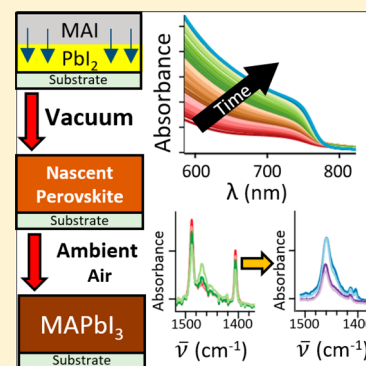
Formation Dynamics of $\text{CH}_3\text{NH}_3\text{PbI}_3$ Perovskite Following Two-Step Layer Deposition

Jay B. Patel, Rebecca L. Milot, Adam D. Wright, Laura M. Herz, and Michael B. Johnston*

Department of Physics, University of Oxford, Clarendon Laboratory, Parks Road, Oxford OX1 3PU, United Kingdom

Supporting Information

ABSTRACT: Hybrid metal-halide perovskites have emerged as a leading class of semiconductors for optoelectronic devices because of their desirable material properties and versatile fabrication methods. However, little is known about the chemical transformations that occur in the initial stages of perovskite crystal formation. Here we follow the real-time formation dynamics of MAPbI_3 from a bilayer of lead iodide (PbI_2) and methylammonium iodide (MAI) deposited through a two-step thermal evaporation process. By lowering the substrate temperature during deposition, we are able to initially inhibit intermixing of the two layers. We subsequently use infrared and visible light transmission, X-ray diffraction, and photoluminescence lifetime measurements to reveal the room-temperature transformations that occur in vacuum and ambient air, as MAI diffuses into the PbI_2 lattice to form MAPbI_3 . In vacuum, the transformation to MAPbI_3 is incomplete as unreacted MAI is retained in the film. However, exposure to moist air allows for conversion of the unreacted MAI to MAPbI_3 , demonstrating that moisture is essential in making MAI more mobile and thus aiding perovskite crystallization. These dynamic processes are reflected in the observed charge-carrier lifetimes, which strongly fluctuate during periods of large ion migration but steadily increase with improving crystallinity.



Inorganic–organic metal-halide perovskites have shown great potential as active materials in optoelectronic devices including photodetectors, LEDs, and solar cells.¹ Many factors make this class of materials exciting for future applications, including large absorption coefficients for visible light, high charge carrier mobilities, long carrier lifetimes, and long diffusion lengths.^{2–4} Furthermore, these perovskites are versatile in terms of band gap tunability, and can be fabricated using a wide range of different methods.⁵ Spin coating techniques offer a facile and low-cost route yielding high quality thin films with high power conversion efficiencies (PCE).⁶ In addition, thermal evaporation is a solvent-free process that has been shown to produce pinhole-free films capable of achieving high PCEs.⁷ This highly controllable process can be used with a wide range of substrates and device architectures, as evaporation is insensitive to dewetting and solubility of precursors.^{8,9} Moreover, such thermal evaporation and spin coating techniques offer multiple synthetic precursor routes to the eventual perovskite formation. Two common precursor pathways are the one-step and two-step deposition methods. For the one-step method, all of the reactants are mixed prior to film deposition (either in solution or in the vapor), whereas in the two-step method the reactants are deposited sequentially.¹⁰

The growth and processing conditions of the perovskite films can greatly affect the PCE of the resultant photovoltaic devices. For example, it is well-established that annealing methylammonium lead iodide (MAPbI_3) films causes more crystalline, uniform films, which enhances the PCE and the general stability of the film.¹¹ Yet, recently, evaporation techniques have

shown that annealing is not mandatory to achieve highly crystalline films.⁸ Similarly, it has been observed that thermally annealing a film in humid environments can have a positive effect on film morphology, crystallinity of the film and device performance.^{12,13} However, such exposure of MAPbI_3 films to moisture has to be carefully balanced, as prolonged periods lead to the formation of lead iodide and hence decomposition of the film.¹⁴ Additionally, moisture in the precursor solutions and in the atmosphere can have a large influence on the crystallinity of the MAPbI_3 film and consequently the attainable PCEs.^{15–17} Another wide parameter space is opened by sequential layer deposition, with the quality of the subsequently formed perovskite depending on temperature and fabrication conditions.^{15,18}

These examples illustrate that the optimization of MAPbI_3 film quality and stability crucially relies on an improved understanding of the chemical and structural transformations that occur during the initial interaction between PbI_2 and MAI. However, investigations of such film formation dynamics have been hampered by the fast interconversion dynamics of PbI_2 with MAI. In the study presented here, we have been able to slow this process by depositing, through thermal evaporation, a thin layer of MAI on an existing layer of PbI_2 at sufficiently low temperature to initially inhibit interdiffusion. After heating of the dual-layer film to room temperature, we subsequently

Received: November 7, 2015

Accepted: December 14, 2015

Published: December 14, 2015

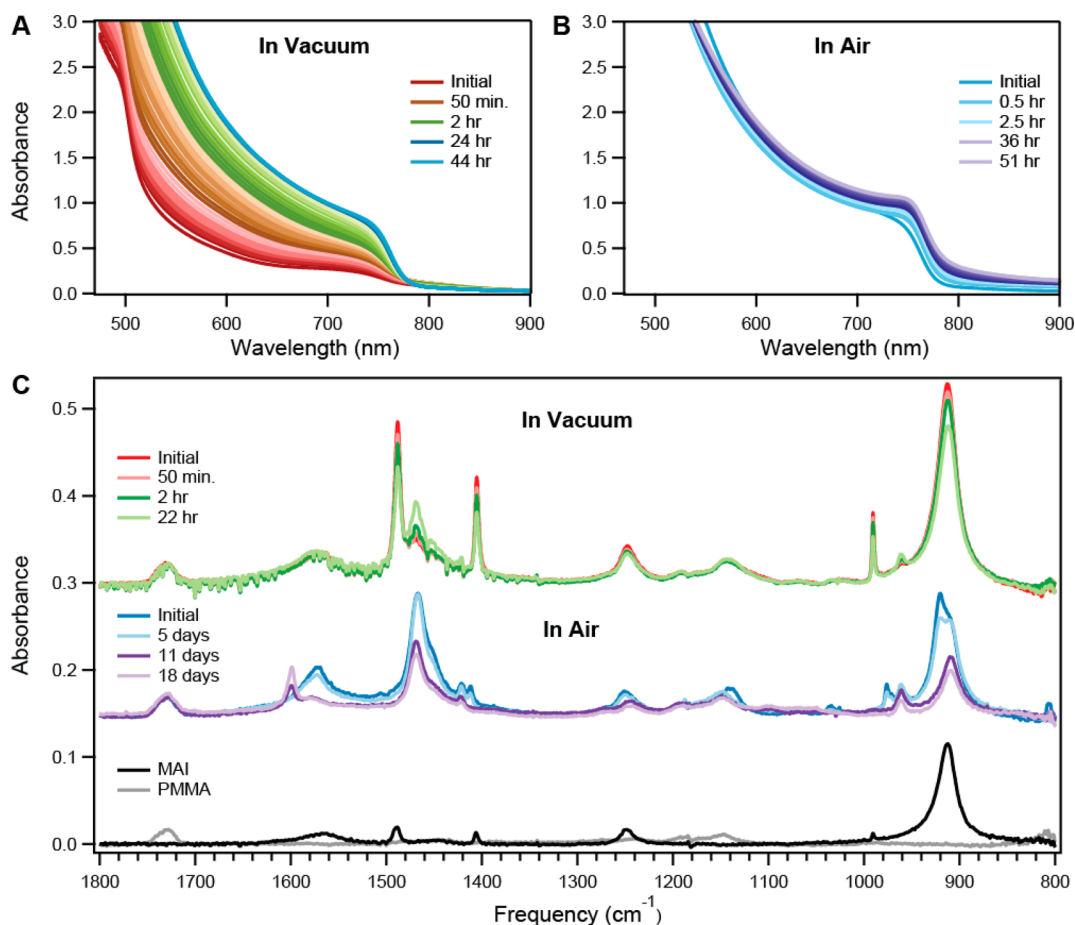


Figure 1. Visible and IR transmission spectra of an initially deposited bilayer MAI/PbI₂ as a function of time. Spectra were taken immediately following heating to room temperature ($21\text{ }^{\circ}\text{C} \pm 1\text{ }^{\circ}\text{C}$), which initiates the formation of MAPbI₃ from MAI and PbI₂. (A) Changes in absorbance in the visible region for films under vacuum, taken for the initial bilayer MAI/PbI₂ (darkest red line), through the progression to a nascent MAPbI₃ perovskite structure over a period of 44 h (lightest blue line). (B) Changes in absorbance in the visible region following the subsequent exposure of the film to ambient air. (C) IR transmission spectra for the bilayer MAI/PbI₂ (red line), the nascent MAPbI₃ perovskite structure formed in vacuum (light green line), and the more crystalline MAPbI₃ following exposure of the film to ambient air (blue line). Assignments of peaks in the IR spectra are provided in Table 1.

monitor the MAPbI₃ formation dynamics in real time using Fourier transform infrared spectroscopy (FTIR), UV–visible absorption spectroscopy, X-ray diffraction (XRD) and transient photoluminescence (PL) measurements. By following the processes occurring first in vacuum, we are able to identify the formation of a nascent MAPbI₃ perovskite structure with regions of unreacted MAI that detracts the film’s optoelectronic properties. We show that subsequent exposure of the film to ambient (humid) air initiates the incorporation of unreacted MAI and enhances crystallinity.

The films were prepared using a two-step thermal evaporation technique optimized to slow the reaction of PbI₂ and MAI during deposition. Lead iodide was evaporated on KBr, glass and z-cut quartz substrates held at $21\text{ }^{\circ}\text{C}$, which were then cooled to $0\text{ }^{\circ}\text{C}$ before MAI was evaporated onto the PbI₂ film. It was essential that both before and during the deposition of the MAI, the temperature of the substrate was kept at $0\text{ }^{\circ}\text{C}$ so that the diffusion of MAI into the PbI₂ layer was minimized prior to measurements commencing. Samples were subsequently investigated at room temperature, which initiated the intermixing of components. PL lifetimes and visible and IR absorption data were initially taken in vacuum to monitor the changes in the film in the absence of ambient air. After 44 h, the

films were then exposed to air, which introduced moisture to the film. Since XRD measurements under vacuum were not possible in our system, the films were sealed with Kapton polyimide sheets here to slow the exposure to ambient air. A detailed description of the experimental techniques can be found in the Supporting Information (SI).

Figure 1 shows the dynamic evolution of IR and visible absorption features of MAI/PbI₂ bilayers following the commencement of interdiffusion in vacuum and subsequent exposure to ambient air. While the bilayers are in vacuum, the most dramatic changes occur in the visible absorbance spectrum (Figure 1A). Within the first 2 h, the PbI₂ absorbance band edge (520 nm) disappears, and the MAPbI₃ band edge begins to establish itself near 750 nm.¹⁹ These changes indicate that the MAI slowly diffuses across the PbI₂ layer and completely disrupts the layered arrays of I–Pb–I (where the stacking arrangement is in the form of a 2 hexagonal-polytype).²⁰ As a result, the formation of the three-dimensional (3D) MAPbI₃ perovskite structure is initiated. Even after the disappearance of PbI₂, however, the MAPbI₃ band edge continues to sharpen and red-shift, and overall absorption increases above the band edge. After 24 h, the MAPbI₃ band

edge is clearly defined, and no further spectral changes are observed.

While changes in the content of PbI_2 and MAPbI_3 leave clear features in the UV/vis absorption spectra, the presence of MAI cannot be as easily inferred because it does not feature significant absorption in this spectral region. We therefore employ IR spectroscopy (Figure 1C), which provides valuable insight into the different chemical environments MAI experiences inside the 3D perovskite cage through the vibrational modes associated with the CH_3NH_3^+ (MA^+) bonds.²¹ Initially, the IR spectrum closely resembles the spectrum for an evaporated film of MAI, and little change is observed in the first 50 min. After 50 min, however, the incorporation of MAI into the MAPbI_3 structure becomes evident from changes in the IR signatures. The vibrations associated with the symmetric NH_3^+ and CH_3 bend (1490 and 1407 cm^{-1} , respectively) in the MAI slowly decrease in intensity, and new peaks corresponding to the same vibrational modes in MAPbI_3 begin to form at 1468 and 1422 cm^{-1} (Table 1). At higher energies, a similar transformation occurs: the

Table 1. Assignment of Infrared (IR) Active Modes in MAI, MAPbI_3 , and the Dihydrate $(\text{CH}_3\text{NH}_3)_4\text{PbI}_6 \cdot 2\text{H}_2\text{O}$

comparison of IR modes		frequency (cm^{-1})		
mode/symmetry	classification	MAI ^a	MAPbI_3 ^b	dihydrate
ν_9/E	asym. NH_3^+ bend	1569	1574	1573
ν_3/A_1	sym. NH_3^+ bend	1490	1468	1466
ν_{10}/E	asym. CH_3 bend	1450	1451	1453
ν_4/A_1	sym. CH_3 bend	1407	1422	1413
				1422
ν_{11}/E	$\text{NH}_3^+/\text{CH}_3$ rock	1251	1252	1255
ν_5/A_1	C–N stretch	990	960	977
ν_{12}/E	$\text{NH}_3^+/\text{CH}_3$ rock	912	910	922

^aMode assignments were made using ref 23. ^bMode assignments were made using ref 21.

C–N stretching vibration of MAI at 990 cm^{-1} decreases in intensity, while the MAPbI_3 peak intensity at 960 cm^{-1} increases. Notably, not all of the initial vibrational modes associated with MAI shift. As can be seen in Table 1 the asymmetric (E) NH_3^+ bend and the NH_3^+ rocking vibrational modes occur at near identical frequencies in MAI and MAPbI_3 .²²

After ~ 22 h of interconversion in vacuum, no further changes are evident in either the IR spectrum (Figure 1C) or the UV/vis absorbance spectra (Figure 1A). However, the IR signatures show that at this stage remnants of MAI-specific peaks are still present, suggesting that a significant amount of MAI has not been incorporated into the MAPbI_3 perovskite structure, despite the 1:1 ratio of PbI_2 :MAI in the initial bilayer film. This may indicate that there are local areas of excess MAI within the film. Figure S1B in the SI also shows the IR spectra of a film that was stored in pure nitrogen (<1 ppm of O_2 , <1 ppm of H_2O) for 30 days. There are still visible signs of MAI within the film, as can be seen by the presence of the C–N stretch mode at 990 cm^{-1} , thus complete conversion to MAPbI_3 has not occurred. Therefore, it is clear that the composition of the film in vacuum is still in a nascent perovskite state despite the well-defined band edge in the visible spectrum and the complete disappearance of all PbI_2

spectral features. These results further support the notion proposed by Yang et al. that perovskite formation is accompanied by the complete breakdown of two-dimensional PbI_2 occurring as a result of MAI infiltration that is then followed by reorientation of MA^+ cations to consequently form the three-dimensional MAPbI_3 structure.²⁴

To explore the role of moisture on the film formation and MAI content, films were exposed to ambient air ($21 \text{ }^\circ\text{C} \pm 1 \text{ }^\circ\text{C}$, relative humidity = $40\% \pm 10\%$) after they had reached a steady state under vacuum. As can be seen in Figure 1B, moisture only causes relatively subtle changes in absorption near the band edge, including a sharpening and slight red shift with time. As we discuss below, these changes can be understood in terms of an enlargement of crystalline domains. The IR spectra, on the other hand, reveal significant rapid changes upon the exposure to moist air (Figure 1C). The peaks associated with the C–N stretch and the symmetric CH_3 and NH_3^+ in MAI (990 cm^{-1} , 1450 and 1569 cm^{-1} respectively) disappear, and only peaks associated with the MA^+ cation within the perovskite are observed, indicating that all of the MAI has rapidly converted. However, at the same time, additional peaks appear at 1415 and 975 cm^{-1} near the symmetric (A_1) CH_3 bend and the C–N stretch, which are known to be highly sensitive to hydrogen bonding of MA^+ .^{22,25} We fabricated both monohydrate crystals ($(\text{CH}_3\text{NH}_3\text{PbI}_3 \cdot \text{H}_2\text{O})$) and dihydrate films ($(\text{CH}_3\text{NH}_3)_4\text{PbI}_6 \cdot 2\text{H}_2\text{O}$) to investigate the incorporation of water into the perovskite structure.^{26,27} We found that the dihydrate (Figure S1C in the SI) exhibited similar IR features at 1415 and 975 cm^{-1} . The dihydrate forms through hydrogen bonding between water and the ammonium constituent of MAI, which causes a distorted NaCl-type crystal structure.²⁸ Furthermore, dihydrates form readily in ambient conditions if there is an excess of MAI in the perovskite film²⁹ because of the hygroscopic nature of MAI.^{30,31} Therefore, we propose that the initial interdiffusion of PbI_2 and MAI in vacuum leads to the formation of nascent MAPbI_3 with remnant unreacted MAI. Upon exposure to air, moisture aids the ion diffusion of MAI leading to formation of MAPbI_3 and the dihydrate $(\text{CH}_3\text{NH}_3)_4\text{PbI}_6 \cdot 2\text{H}_2\text{O}$. However, perovskite formation proceeds further, and after 11 days, the dihydrate peaks are no longer visible. Once the MAI is consumed, the equilibrium, which is affected by humidity and other environmental factors, shifts to favor the exclusive formation of MAPbI_3 without dihydrate inclusions.^{14,26,32} Furthermore, the shift in equilibrium leads to dissociation of H_2O into the film, which initiates the degradation of the MAPbI_3 (Figure S1D).

We further confirm the occurrence of these chemical and structural changes with X-ray diffraction measurements. Figure 2 shows the changes in XRD spectra over a period of 30 h as the bilayer MAI/ PbI_2 film is converted into a MAPbI_3 film. It must be noted that, because the encapsulated film is slowly being exposed to ambient air throughout the entire experiment, the film formation dynamics are somewhat different in this particular experiment, and therefore only a qualitative comparison with the IR, visible, and PL measurements is possible. XRD measurements show that as expected, a significant quantity of PbI_2 ($2\theta = 12.6^\circ$) and MAI ($2\theta = 19.7^\circ$) is initially present in the film, reflecting the initial bilayer structure created by thermal evaporation. There is also already a strong (110) reflection corresponding to MAPbI_3 (at $2\theta = 14.1^\circ$) due to the crystallization of MAPbI_3 at the interface of the bilayers when the film is heated to room temperature. After 30 min, the PbI_2 reflection ($2\theta = 12.6^\circ$) disappears, while the

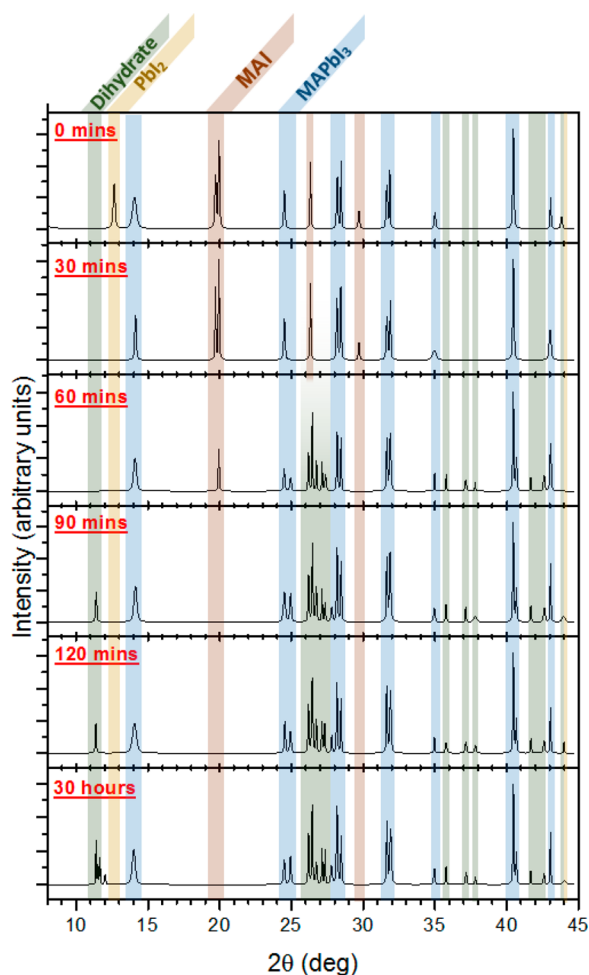


Figure 2. X-ray diffraction patterns following the evolution of MAPbI₃ from the initial bilayer MAI/PbI₂ films (0 min), to the nascent perovskite (30 min), and then finally MAPbI₃ film (90 min). After 90 min, the dihydrate (CH₃NH₃)₄PbI₆·2H₂O is observed to form ($2\theta = 11.4^\circ$, 11.5° , and 11.6°). The films were sealed with Kapton polyimide sheets to slow the exposure to ambient air. Diffraction patterns for individual compounds used for identification can be found in Figure S3 in the SI.

MAI reflections persist, similar to the formation dynamics under vacuum discussed above. Unlike the reference spectra of the individual thin films in Figure S2, the spectra for the dynamic bilayer film show subtle differences. This can be attributed to the fact that the bilayer film has a mixture of PbI₂, MAI, and MAPbI₃. Sixty minutes after the disappearance of PbI₂, the MAI reflections also vanish, and a reflection at $2\theta = 11.6^\circ$ appears, which is consistent with the theoretical pattern obtained for the dihydrate.²⁶ Furthermore, after 30 h, due to the crystallization of the dihydrate and the MAPbI₃, sharpening of the reflections of MAPbI₃ occur,³³ and lower intensity reflections ($2\theta = 11.4^\circ$ and 11.5°) of the dihydrate appear.³³ This strongly indicates that the dihydrate and the MAPbI₃ form strong crystalline domains within the film. These XRD spectra hence present further evidence of the importance of moisture, and its role in aiding MAI to be more mobile. We note that while monohydrates have previously been observed to form in MAPbI₃ in the presence of moisture,²⁶ our comparison with the diffraction pattern obtained from monohydrate crystals (Figure S2 in the SI) suggest that the monohydrate species is

insignificant here, with clear contributions only arising from the dihydrate.

Previous studies have shown that the crystal structure of MAPbI₃ is highly amenable to the inclusion of molecules of particular size and polarity, such as NH₃ and CH₃NH₂, which can form crystal structures similar to that of the dihydrate.^{34,35} Accordingly, we observe that the dihydrate is soluble in 2-propanol (IPA), which allows it to be washed from the film (see Figure S3 in the SI), indicating that it is similar in solubility to MAI. Our observations help to explain why removal of excess organic component has proven to be beneficial in solar cell efficiencies.^{36,37} It is clear that, to achieve the highest quality MAPbI₃ films, unreacted MAI needs to be solvated by a solvent of suitable polarity and molecular size, which infiltrates the crystal lattice and ensures either that a proper crystal structure forms, or unwanted molecules such as dihydrates are removed. These hydrates could potentially be detrimental as they can eventually decompose to form liquid water and PbI₂, which causes MAPbI₃ film degradation.^{26,32}

With the complex chemical changes identified, we now analyze how these changes affect the optoelectronic properties of the film. Here, we examine photoluminescence lifetimes τ_{av} and band edge absorption features during film formation (Figure 3), which are sensitive probes of charge-carrier trap density and film crystallinity. The first few hours of PbI₂/MAI bilayer interdiffusion in vacuum are marked by high trap densities and fluctuations: τ_{av} varies erratically (Figure 3A), and the absorption onset is considerably broadened (Figure 3C). These fluctuations are unsurprising considering that the greatest amount of ion movement occurs during this time period, which creates considerable disorder in the crystalline domains.³⁸ As a result, this intermediate phase of perovskite formation is associated with a high density of subgap trap states, as indicated by short photoluminescence lifetimes (Figure 3A) and considerable absorbance at 800 nm, just below the band gap onset (Figure 3B). Over the ensuing 7 h in vacuum, this subgap absorbance then decreases, coinciding with the stabilization of the PL lifetimes, in accordance with a decrease in trap density as the film forms. Over the initial 10 h in vacuum, the band edge of the as-formed MAPbI₃ continuously red shifts and sharpens (Figure 3C,D) indicating that mass diffusion of MAI is followed by the formation of nucleation sites and then the crystallization of MAPbI₃, in analogy with crystallization dynamics reported from real-time XRD.³⁹ Following this initial period of rapid film transformation, the progression of changes begins to slow. PL lifetimes continue to increase, and the band edge continues to red shift and sharpen as the overall crystallinity of the film improves and larger crystalline domains form.

The subsequent exposure to air triggers further changes in optoelectronic properties. Figure 3A shows that the PL lifetimes initially decrease sharply, suggesting that exposure to moisture initially leads to the formation of further trap states. We attribute this effect to the organic species becoming more mobile through exposure to moisture, which again temporarily disrupts the crystal structure. The matching IR and XRD measurements discussed above suggest that exposure to ambient air leads to an increase in MAI diffusion and a faster crystallization process.⁴⁰ After about 5 h, however, these rapid transformations settle and the PL lifetime increases substantially in accordance with improved material quality. Concomitantly, the width of the band edge sharpens (Figure 3C) and the band edge shifts to the red (Figure 3D). These changes

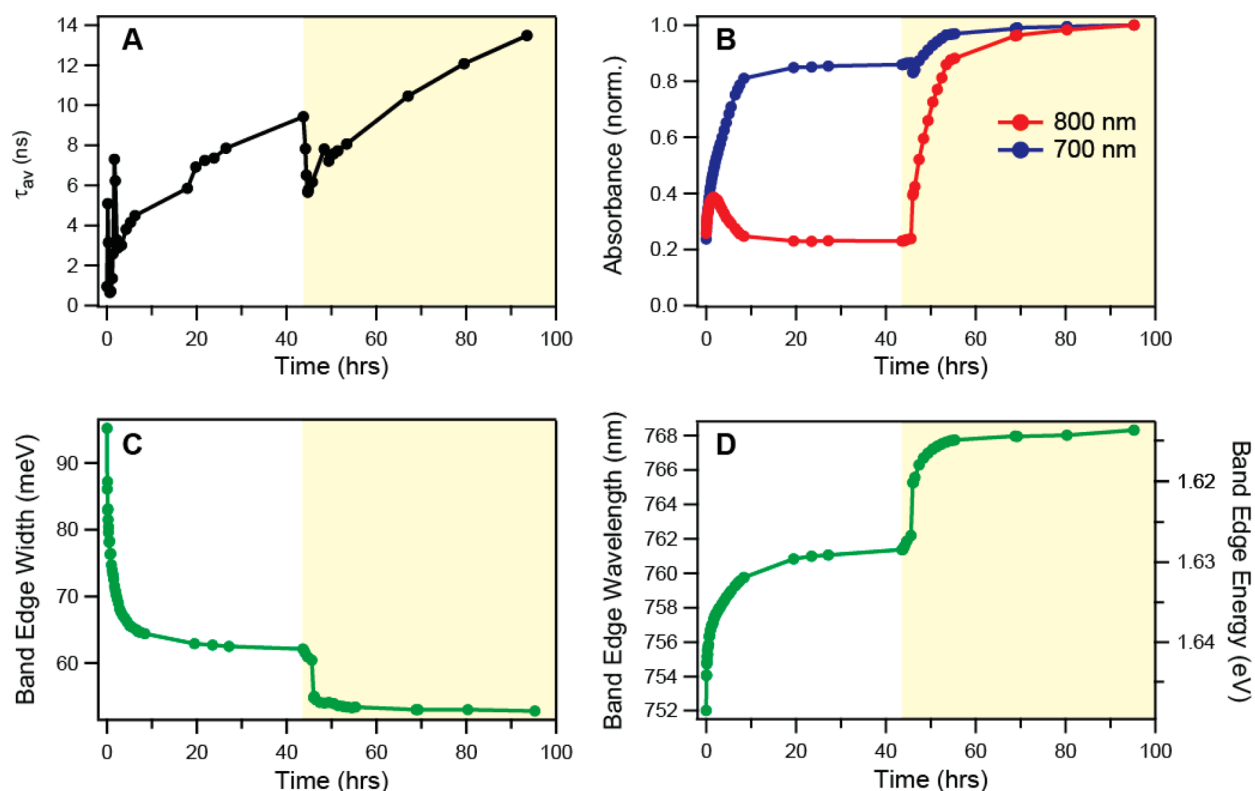


Figure 3. (A) Time-resolved PL lifetime as a function of time from the initial deposition of the MAI/PbI₂ bilayer to the formation of MAPbI₃, both in vacuum (white) and after exposure to ambient air (yellow shading). Details of calculations of τ_{av} and raw PL data are provided in the SI. (B) Changes in absorbance at wavelengths of 700 and 800 nm derived from the initial absorption spectra (Figure 1A,B). (C) Width of the band edge absorption onset, determined from the full-width half-maximum of a Gaussian fit to the derivative spectrum. (D) Band edge wavelength and energy obtained from Gaussian fits to the differential absorption spectra. Values correspond approximately to the midpoint of the band gap absorption feature.

hence result from moisture-driven enhancement of material crystallinity that leads to larger domain sizes,⁴¹ in analogy to previous studies correlating grain- and crystal-size with changes in absorption onset in MAPbI₃.³⁹ We note that while the nominal absorbance below the bandgap (800 nm, Figure 3B) appears to increase during this crystallization phase, this is most likely caused by enhanced light scattering effects, which become stronger as smaller (subwavelength) crystalline domains combine to form larger domains.

In summary, through careful control of substrate temperature during growth, we have been able to monitor in real time the chemical transformations evolving as MAI diffuses into PbI₂ to form a MAPbI₃ perovskite film. The changes occurring in either vacuum or ambient air shed light on key parameters that need to be controlled to create a high quality perovskite film. We present clear evidence from visible and IR transmission spectra that, in vacuum, MAI and PbI₂ interdiffuse to form a nascent MAPbI₃ perovskite structure. However, ambient air is required to fully crystallize MAPbI₃ and remove excess MAI. The hygroscopic nature of MAI allows it to absorb moisture, making it more mobile and allowing for better intermixing of PbI₂ and MAI. It is, however, found to be essential that no excess MAI remains within the film, as the unreacted MAI absorbs moisture to form the dihydrate (CH₃NH₃)₄PbI₆·2H₂O, which is a relatively stable crystalline material in itself. Furthermore, we show that after a certain period of time, chemical and optoelectronic changes with exposure to moisture cease, and therefore any further moisture absorption is likely to be detrimental. We further correlate these dynamic material

changes with the corresponding evolution of charge-carrier lifetimes and absorption features, identifying dynamic periods of high ion motion and high trap densities and observing the effect of moisture in driving crystallization. These findings provide fundamental insight into the dynamics of perovskite formation. Importantly, they also highlight the role that moisture has to play in ensuring the complete reaction of the precursor materials, thus leading to the formation of strong crystalline MAPbI₃, which is crucial for optimal solar cell performance.

■ ASSOCIATED CONTENT

📄 Supporting Information

The Supporting Information is available free of charge on the ACS Publications website at DOI: 10.1021/acs.jpcllett.5b02495.

Detailed information on sample preparation and experimental techniques, along with additional MIR spectra and XRD patterns of the MAPbI₃, hydrates, and precursors (PDF)

■ AUTHOR INFORMATION

Corresponding Author

*E-mail: michael.johnston@physics.ox.ac.uk

Notes

The authors declare no competing financial interest.

ACKNOWLEDGMENTS

We gratefully acknowledge financial support from the Engineering and Physical Sciences Research Council (U.K.) (EPSRC). We thank Dr. D. Prabhakaran for experimental support with XRD measurements. J.B.P. thanks the EPSRC and Merck Chemicals for financial support through an Industrial CASE studentship. A.D.W. thanks the EPSRC for funding via the Centre for Doctoral Training in Plastic Electronic Materials.

REFERENCES

- (1) Stranks, S. D.; Snaith, H. J. Metal-Halide Perovskites for Photovoltaic and Light-Emitting Devices. *Nat. Nanotechnol.* **2015**, *10* (5), 391–402.
- (2) Wehrenfennig, C.; Eperon, G. E.; Johnston, M. B.; Snaith, H. J.; Herz, L. M. High Charge Carrier Mobilities and Lifetimes in Organolead Trihalide Perovskites. *Adv. Mater.* **2014**, *26* (10), 1584–1589.
- (3) Wehrenfennig, C.; Liu, M.; Snaith, H. J.; Johnston, M. B.; Herz, L. M. Charge-Carrier Dynamics in Vapour-Deposited Films of the Organolead Halide Perovskite $\text{CH}_3\text{NH}_3\text{PbI}_{3-x}\text{Cl}_x$. *Energy Environ. Sci.* **2014**, *7* (7), 2269.
- (4) Stranks, S. D.; Eperon, G. E.; Grancini, G.; Menelaou, C.; Alcocer, M. J. P.; Leijtens, T.; Herz, L. M.; Petrozza, A.; Snaith, H. J. Electron-Hole Diffusion Lengths Exceeding 1 Micrometer in an Organometal Trihalide Perovskite Absorber. *Science* **2013**, *342* (6156), 341–344.
- (5) Eperon, G. E.; Stranks, S. D.; Menelaou, C.; Johnston, M. B.; Herz, L. M.; Snaith, H. J. Formamidinium Lead Trihalide: A Broadly Tunable Perovskite for Efficient Planar Heterojunction Solar Cells. *Energy Environ. Sci.* **2014**, *7* (3), 982.
- (6) Yang, W. S.; Noh, J. H.; Jeon, N. J.; Kim, Y. C.; Ryu, S.; Seo, J.; Seok, S. I. High-Performance Photovoltaic Perovskite Layers Fabricated through Intramolecular Exchange. *Science* **2015**, *348* (6240), 1234–1237.
- (7) Liu, M.; Johnston, M. B.; Snaith, H. J. Efficient Planar Heterojunction Perovskite Solar Cells by Vapour Deposition. *Nature* **2013**, *501* (7467), 395–398.
- (8) Lin, Q.; Armin, A.; Nagiri, R. C. R.; Burn, P. L.; Meredith, P. Electro-Optics of Perovskite Solar Cells. *Nat. Photonics* **2014**, *9* (2), 106–112.
- (9) Stranks, S. D.; Wood, S. M.; Wojciechowski, K.; Deschler, F.; Saliba, M.; Khandelwal, H.; Patel, J. B.; Elston, S. J.; Herz, L. M.; Johnston, M. B.; et al. Enhanced Amplified Spontaneous Emission in Perovskites Using a Flexible Cholesteric Liquid Crystal Reflector. *Nano Lett.* **2015**, *15* (8), 4935–4941.
- (10) Im, J.-H.; Kim, H.-S.; Park, N.-G. Morphology-Photovoltaic Property Correlation in Perovskite Solar Cells: One-Step versus Two-Step Deposition of $\text{CH}_3\text{NH}_3\text{PbI}_3$. *APL Mater.* **2014**, *2* (8), 081510.
- (11) Dualeh, A.; Tétreault, N.; Moehl, T.; Gao, P.; Nazeeruddin, M. K.; Grätzel, M. Effect of Annealing Temperature on Film Morphology of Organic-Inorganic Hybrid Perovskite Solid-State Solar Cells. *Adv. Funct. Mater.* **2014**, *24* (21), 3250–3258.
- (12) You, J.; Yang, Y. (M.); Hong, Z.; Song, T.-B.; Meng, L.; Liu, Y.; Jiang, C.; Zhou, H.; Chang, W.-H.; Li, G.; et al. Moisture Assisted Perovskite Film Growth for High Performance Solar Cells. *Appl. Phys. Lett.* **2014**, *105* (18), 183902.
- (13) Gao, H.; Bao, C.; Li, F.; Yu, T.; Yang, J.; Zhu, W.; Zhou, X.; Fu, G.; Zou, Z. Nucleation and Crystal Growth of Organic-Inorganic Lead Halide Perovskites under Different Relative Humidity. *ACS Appl. Mater. Interfaces* **2015**, *7* (17), 9110–9117.
- (14) Christians, J. A.; Miranda Herrera, P. A.; Kamat, P. V. Transformation of the Excited State and Photovoltaic Efficiency of $\text{CH}_3\text{NH}_3\text{PbI}_3$ Perovskite upon Controlled Exposure to Humidified Air. *J. Am. Chem. Soc.* **2015**, *137* (4), 1530–1538.
- (15) Ko, H.-S.; Lee, J.-W.; Park, N.-G. 15.76% Efficiency Perovskite Solar Cells Prepared under High Relative Humidity: Importance of PbI_2 Morphology in Two-Step Deposition of $\text{CH}_3\text{NH}_3\text{PbI}_3$. *J. Mater. Chem. A* **2015**, *3* (16), 8808–8815.
- (16) Wu, C.-G.; Chiang, C.-H.; Tseng, Z.-L.; Nazeeruddin, M. K.; Hagfeldt, A.; Grätzel, M. High Efficiency Stable Inverted Perovskite Solar Cells without Current Hysteresis. *Energy Environ. Sci.* **2015**, *8* (9), 2725–2733.
- (17) Gong, X.; Li, M.; Shi, X.-B.; Ma, H.; Wang, Z.-K.; Liao, L.-S. Controllable Perovskite Crystallization by Water Additive for High-Performance Solar Cells. *Adv. Funct. Mater.* **2015**, *25* (42), 6671–6678.
- (18) Ahn, N.; Son, D.-Y.; Jang, I.-H.; Kang, S. M.; Choi, M.; Park, N.-G. Highly Reproducible Perovskite Solar Cells with Average Efficiency of 18.3% and Best Efficiency of 19.7% Fabricated via Lewis Base Adduct of Lead(II) Iodide. *J. Am. Chem. Soc.* **2015**, *137* (27), 8696–8699.
- (19) Milot, R. L.; Eperon, G. E.; Snaith, H. J.; Johnston, M. B.; Herz, L. M. Temperature-Dependent Charge-Carrier Dynamics in $\text{CH}_3\text{NH}_3\text{PbI}_3$ Perovskite Thin Films. *Adv. Funct. Mater.* **2015**, *25* (39), 6218–6227.
- (20) Beckmann, P. A. A Review of Polyttypism in Lead Iodide. *Cryst. Res. Technol.* **2010**, *45* (5), 455–460.
- (21) Pérez-Osorio, M. A.; Milot, R. L.; Filip, M. R.; Patel, J. B.; Herz, L. M.; Johnston, M. B.; Giustino, F. Vibrational Properties of the Organic-Inorganic Halide Perovskite $\text{CH}_3\text{NH}_3\text{PbI}_3$ from Theory and Experiment: Factor Group Analysis, First-Principles Calculations, and Low-Temperature Infrared Spectra. *J. Phys. Chem. C* **2015**, *119* (46), 25703–25718.
- (22) Whalley, E. Infrared Spectra of the Methylammonium Halides: Effects of Orientational Disorder about One Axis. *J. Chem. Phys.* **1969**, *51* (9), 4040.
- (23) Cabana, A.; Sandorfy, C. The Infrared Spectra of Solid Methylammonium Halides. *Spectrochim. Acta* **1962**, *18* (4), 843–861.
- (24) Yang, S.; Zheng, Y. C.; Hou, Y.; Chen, X.; Chen, Y.; Wang, Y.; Zhao, H.; Yang, H. G. Formation Mechanism of Freestanding $\text{CH}_3\text{NH}_3\text{PbI}_3$ Functional Crystals: In Situ Transformation vs Dissolution–Crystallization. *Chem. Mater.* **2014**, *26* (23), 6705–6710.
- (25) Mosconi, E.; Quarti, C.; Ivanovska, T.; Ruani, G.; De Angelis, F. Structural and Electronic Properties of Organo-Halide Lead Perovskites: A Combined IR-Spectroscopy and Ab Initio Molecular Dynamics Investigation. *Phys. Chem. Chem. Phys.* **2014**, *16* (30), 16137.
- (26) Leguy, A. M. A.; Hu, Y.; Campoy-Quiles, M.; Alonso, M. I.; Weber, O. J.; Azarhoosh, P.; van Schilfhaarde, M.; Weller, M. T.; Bein, T.; Nelson, J.; et al. Reversible Hydration of $\text{CH}_3\text{NH}_3\text{PbI}_3$ in Films, Single Crystals, and Solar Cells. *Chem. Mater.* **2015**, *27* (9), 3397–3407.
- (27) Manser, J. S.; Reid, B.; Kamat, P. V. Evolution of Organic-Inorganic Lead Halide Perovskite from Solid-State Iodoplumbate Complexes. *J. Phys. Chem. C* **2015**, *119* (30), 17065–17073.
- (28) Vincent, B. R.; Robertson, K. N.; Cameron, T. S.; Knop, O. Alkylammonium Lead Halides. Part 1. Isolated PbI_6 4- Ions in $(\text{CH}_3\text{NH}_3\text{PbI}_3)_4 \text{PbI}_6 \cdot 2\text{H}_2\text{O}$. *Can. J. Chem.* **1987**, *65* (5), 1042–1046.
- (29) Halder, A.; Choudhury, D.; Ghosh, S.; Subbiah, A. S.; Sarkar, S. K. Exploring Thermochromic Behavior of Hydrated Hybrid Perovskites in Solar Cells. *J. Phys. Chem. Lett.* **2015**, *6* (16), 3180–3184.
- (30) Zhou, H.; Chen, Q.; Li, G.; Luo, S.; Song, T.-b.; Duan, H.-S.; Hong, Z.; You, J.; Liu, Y.; Yang, Y. Interface Engineering of Highly Efficient Perovskite Solar Cells. *Science* **2014**, *345* (6196), 542–546.
- (31) Eperon, G. E.; Habisreutinger, S. N.; Leijtens, T.; Bruijnsaers, B. J.; van Franeker, J. J.; DeQuilettes, D. W.; Pathak, S.; Sutton, R. J.; Grancini, G.; Ginger, D. S.; et al. The Importance of Moisture in Hybrid Lead Halide Perovskite Thin Film Fabrication. *ACS Nano* **2015**, *9* (9), 9380–9393.
- (32) Imler, G. H.; Li, X.; Xu, B.; Dobereiner, G. E.; Dai, H.-L.; Rao, Y.; Wayland, B. B. Solid State Transformation of the Crystalline Monohydrate $(\text{CH}_3\text{NH}_3)\text{PbI}_3 \cdot (\text{H}_2\text{O})$ to the $(\text{CH}_3\text{NH}_3)\text{PbI}_3$ Perovskite. *Chem. Commun.* **2015**, *51* (56), 11290–11292.
- (33) Baikie, T.; Fang, Y.; Kadro, J. M.; Schreyer, M.; Wei, F.; Mhaisalkar, S. G.; Graetzel, M.; White, T. J. Synthesis and Crystal Chemistry of the Hybrid Perovskite $(\text{CH}_3\text{NH}_3)\text{PbI}_3$ for Solid-State

Sensitised Solar Cell Applications. *J. Mater. Chem. A* **2013**, *1* (18), 5628.

(34) Zhou, Z.; Wang, Z.; Zhou, Y.; Pang, S.; Wang, D.; Xu, H.; Liu, Z.; Padture, N. P.; Cui, G. Methylamine-Gas-Induced Defect-Healing Behavior of $\text{CH}_3\text{NH}_3\text{PbI}_3$ Thin Films for Perovskite Solar Cells. *Angew. Chem., Int. Ed.* **2015**, *54* (33), 9705–9709.

(35) Zhao, Y.; Zhu, K. Optical Bleaching of Perovskite (CH_3NH_3)- PbI_3 through Room-Temperature Phase Transformation Induced by Ammonia. *Chem. Commun. (Cambridge, U. K.)* **2014**, *50* (13), 1605–1607.

(36) Wakamiya, A.; Endo, M.; Sasamori, T.; Tokitoh, N.; Ogomi, Y.; Hayase, S.; Murata, Y. Reproducible Fabrication of Efficient Perovskite-Based Solar Cells: X-Ray Crystallographic Studies on the Formation of $\text{CH}_3\text{NH}_3\text{PbI}_3$ Layers. *Chem. Lett.* **2014**, *43* (5), 711–713.

(37) Wang, X.; Li, X.; Tang, G.; Zhao, L.; Zhang, W.; Jiu, T.; Fang, J. Improving Efficiency of Planar Hybrid $\text{CH}_3\text{NH}_3\text{PbI}_{3-x}\text{Cl}_x$ Perovskite Solar Cells by Isopropanol Solvent Treatment. *Org. Electron.* **2015**, *24*, 205–211.

(38) Pathak, S.; Sepe, A.; Sadhanala, A.; Deschler, F.; Haghighirad, A.; Sakai, N.; Goedel, K. C.; Stranks, S. D.; Noel, N.; Price, M.; et al. Atmospheric Influence upon Crystallization and Electronic Disorder and Its Impact on the Photophysical Properties of Organic–Inorganic Perovskite Solar Cells. *ACS Nano* **2015**, *9* (3), 2311–2320.

(39) Miyadera, T.; Shibata, Y.; Koganezawa, T.; Murakami, T. N.; Sugita, T.; Tanigaki, N.; Chikamatsu, M. Crystallization Dynamics of Organolead Halide Perovskite by Real-Time X-Ray Diffraction. *Nano Lett.* **2015**, *15* (8), 5630–5634.

(40) Bass, K. K.; McAnally, R. E.; Zhou, S.; Djurovich, P. I.; Thompson, M. E.; Melot, B. C. Influence of Moisture on the Preparation, Crystal Structure, and Photophysical Properties of Organohalide Perovskites. *Chem. Commun.* **2014**, *50* (99), 15819–15822.

(41) D'Innocenzo, V.; Grancini, G.; Alcocer, M. J. P.; Kandada, A. R. S.; Stranks, S. D.; Lee, M. M.; Lanzani, G.; Snaith, H. J.; Petrozza, A. Excitons versus Free Charges in Organo-Lead Tri-Halide Perovskites. *Nat. Commun.* **2014**, *5*, 3586.